Available online at www.eccomasproceedia.org
Eccomas Proceedia SMART (2023) 1076-1087

ECCOMAS
Proceedia

X ECCOMAS Thematic Conference on Smart Structures and Materials
SMART 2023
D.A. Saravanos, A. Benjeddou, N. Chrysochoidis and T. Theodosiou (Eds)

DYNAMIC STRAIN VERSUS ACCELERATION BASED ROBUST STRUCTURAL HEALTH MONITORING FOR A GROUP OF COMPOSITE AEROSTRUCTURES: EXPERIMENTAL ASSESSMENT

FATION T. FERA*, PANAYOTIS E. SPILIOTOPOULOS*, IOANNIS E. SARAMANTAS*, YOAV OFIR†, IDDO KRESSEL†, SPILIOS D. FASSOIS*, JOHN S. SAKELLARIOU*, MOSHE TUR§, CHRISTOS SPANDONIDIS‡

*Stochastic Mechanical Systems and Automation (SMSA) Laboratory
University of Patras, 26504 Patras, Greece
e-mail: fationfera@upnet.gr (FTF), p.spiliotop@upnet.gr (PES), jsar@upnet.gr (IES)
fassois@upatras.gr (SDF), sakj@upatras.gr (JSS)

†Advanced Structural Technologies, Engineering and Development Center, Aviation Group,
Israel Aerospace Industries (IAI)
Ben Gurion International Airport, 70100, Israel
e-mail: yoaofir@iai.co.il (YO), ikressel@iai.co.il (IK)

§Tel Aviv University
Ramat Aviv 69978, Israel
e-mail: tur@tauex.tau.ac.il (MT)

‡Prisma Electronics S.A.
87 Dimokratias Avenue, 68100, Alexandroupolis, Greece
e-mail: c.spandonidis@prismael.com (CS)

Key words: Vibration-Based SHM, Data-Based Methods, Robust SHM, Population-Based SHM, Dynamic Strain, Composite Structures

Abstract. The problem of population-based Structural Health Monitoring for composite aerostructures via dynamic strain signals is experimentally investigated under high levels of population, experimental, and temperature uncertainty. Both delamination and impact induced damage are considered using robust data-based methods. Due to the 'small' sample of coupons available for training, the study focuses on assessing the diagnostic performance that would be achievable under training with an adequately large sample of the underlying population. The results demonstrate that high diagnostic performance, reaching a detection accuracy of 99.4% and almost perfect Delamination/Impact damage characterization, is potentially achievable. A comparison with vibration acceleration signals indicates largely similar performance for the considered damages.

Peer-review under responsibility of the organizing committee of SMART 2023.
doi: 10.7712/150123.9858.450606

1 INTRODUCTION

As the importance of Structural Health Monitoring (SHM) for composite structures in the aerospace, energy, and other industries is growing, the use of dynamic strain signals over vibration acceleration counterparts receives increasing attention. This is also motivated by the technological developments and advantages offered by Fiber Bragg Gratings (FBG) technology [1, 2].

This attention has been reflected in a number of recent studies. For instance, in [3] very good damage detection results (detection accuracy of 98.1%) are reported for a UAV structure using Principal Component Analysis based statistics (Q and T^2 indices) and a Self Organizing Map (SOM) cluster algorithm accounting for in-flight excitation variability. Studies exploring artificial damage (added masses) diagnosis[1] on a *single* composite aerostructure via Support Vector Machines (SVM), following a feature extraction procedure based on the discrete wavelet transform [4] or the Fourier transform [5], are reported with detection accuracy higher than 90% and classification efficiency reaching 99.3%. The use of Convolutional Neural Networks for accounting for flight load (excitation) variability is reported in [6] with excellent accuracy reaching 99% for detection and 83% for localization using a simulated composite wing.

In [7] superiority of dynamic strain based damage detection over vibration acceleration based is claimed via the use of modal shapes, although this refers to a metallic beam. In [8], the presence of artificial damages (added masses) on a metallic structure is revealed via discrepancies in Frequency Response Functions (FRFs), with strain FRFs exhibiting improved sensitivity to damage over their acceleration counterparts. In [9] the feasibility of strain based damage detection on a numerical store frame and a metallic circular arch is reported via a damage index robust to excitation (although measurement of the excitation is required).

Despite the progress achieved thus far, the question of dynamic strain based damage diagnosis effectiveness for composite aerostructures, in particular under *unobservable* excitation and in comparison to vibration acceleration based diagnosis, remains an important research topic. Even more so under population and other uncertainty factors which are well known to have serious detrimental consequences [1]. This precise problem has been at the focus of our parallel study [10] which is based on Monte Carlo numerical experiments with a population sample of 90 composite aerostructures, under manufacturing and temperature uncertainty, simulated via Finite Element Models. As demonstrated therein, high detection (up to 99.2%) but rather low (up to 65.7%) damage type (delamination/debonding) characterization performance is possible via the use of strain-based robust to uncertainty methods. Yet, for 'low' level damage dynamic strain based diagnosis performance is generally lower than that achieved by vibration acceleration based methods.

This work constitutes a parallel to our study [10], in that it *experimentally* explores the performance limits of dynamic strain based damage diagnosis under various uncertainty factors, that is population (mainly due to materials and manufacturing), test rig (experimental), excitation profile, and temperature uncertainty. A comparison with vibration acceleration based diagnosis is also presented. The work is based on a population sample of C-shaped composite coupons manufactured by the Israel Aeronautical Industries (IAI) under the framework of the joint Greece-Israel REALISM research project. A particular challenge, unique to this study, is

[1]The term damage diagnosis is meant to include both detection and characterization.

the fact that it is based on a particularly 'small' population sample (only 26 coupons). The detrimental implication of this is that robust SHM methods *cannot* be adequately trained to properly include the significant (see subsection 2.2) population and other uncertainty present.

Yet, as the question of interest mainly is on the diagnostic performance achievable if a *sufficiently large* sample of the population were available, the study focuses right on this by selecting the *best* (most representative, for instance in the sense of optimizing performance) set of available coupons to include in the methods' Baseline Phase, leaving the remaining coupons for the Inspection Phase (details in section 4).

The rest of this paper is organized as follows: The coupons, the uncertainty factors, and the damage scenarios are discussed in section 2, while brief remarks on the robust to uncertainty damage diagnosis methods employed are made in section 3. Performance assessment and comparisons with vibration acceleration based SHM are presented in section 4, and concluding remarks are summarized in section 5.

2 THE COUPONS, THE UNCERTAINTY FACTORS, THE DAMAGE SCENARIOS, AND THEIR EFFECTS ON THE DYNAMICS

2.1 The coupons and the experimental set-up

The experiments are carried out using a set of 26 C-shaped composite coupons, each one consisting of twelve carbon fiber epoxy resin laminates with $[0/45_2/0/45/0]_S$ ply architecture. The cross-section dimensions are 25.0×81.8 mm and the total length is 860.1 mm. The ply properties have been experimentally determined, with their values being summarized in Table 1.

Twenty coupons are in pristine condition, four under Delamination damage, and two under Impact-induced damage, with each coupon assigned an ID tag. These IDs are $1 \ldots 20$ for the pristine coupons, $21, 22$ and $25, 26$ for the 'Low' and 'High' Delamination coupons, respectively, and 27 and 30 for 'Low' and 'High' Impact damage coupons, respectively.

A picture of the experimental set-up organized at the University of Patras, Greece, is provided in Figure 1, and a corresponding schematic representation in Figure 2. As indicated, each coupon is clamped at one end via 4 screws (clamping torque of 1.6 Nm) while being free at the other end. It is excited at two distinct locations (E1 and E2), while strain and acceleration measurements are acquired in the indicated directions at three locations (locations 1, 2, 3). The set-up is operated within a freezer allowing for temperature variation (measured via a K-type thermocouple) between experiments.

2.2 The uncertainty factors and their effects on the dynamics

Four main uncertainty factors are present: (a) Material and manufacturing uncertainty, (b) experimental set-up uncertainty (due to clamping and excitation/sensor location), (c) random force excitation profile uncertainty, and (d) temperature uncertainty (within the $[0 \ldots 25]\,^oC$ range). The first one concerns population uncertainty and the subsequent three correspond to varying Environmental and Operational Conditions (EOCs).

The effects of temperature uncertainty (6 temperatures for Coupon 1, 5 curves per temperature) and the combined material, manufacturing, and set-up uncertainty on the pristine dynamics (all 20 pristine coupons at $25\,^oC$; 5 curves per coupon), always under the additional random excitation profile uncertainty, are depicted in Figure 3 via the Transmittance Function

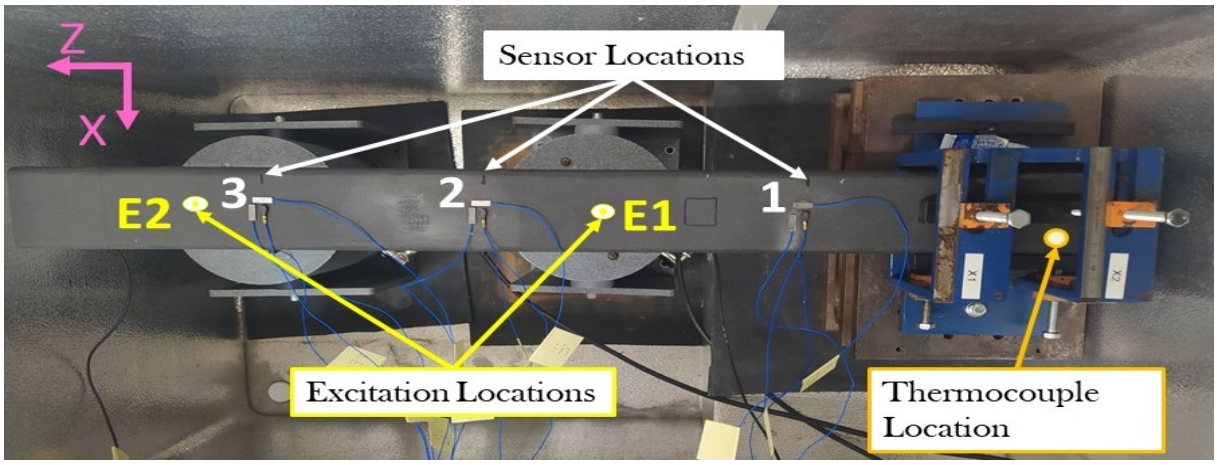

Figure 1: Photo of the experimental set-up (top view): Sensor, excitation, and thermocouple locations are indicated by arrows [11].

$S2^Z/S1^Z$ Welch-based magnitude estimates for the pristine structures (symbol explanations in Figure 2). It should be noted that throughout this study the term dynamics refers to the partial structural dynamics as reflected in the strain (or acceleration) based Multiple-Input Single-Output Transmittance Function (MISO-TF) employing the signals at locations 1 and 3 as pseudo-inputs and that at location 2 as output.

Based on Figure 3, the temperature uncertainty effects on the pristine dynamics are important, yet, those of the combined material, manufacturing, and set-up uncertainty are severe. This fact is indicative of the challenging nature of the problem being tackled and further underlines the statement made on the low number of sample structures available.

2.3 The damage scenarios and their effects on the dynamics

As previously indicated, four damage scenarios are considered: 'Low' and 'High' Delamination (designated as DL_L and DL_H, respectively) and 'Low' and 'High' Impact (designated as I_L and I_H); details in Table 2.

Delamination (DL) damage is implemented using a square-shaped layer of Teflon placed

Coupon Details	
Material	Carbon Epoxy
Young's Modulus E11 (Pa)	5.78×10^{10}
Young's Modulus E22 (Pa)	5.60×10^{10}
Shear Modulus G12 (Pa)	3.87×10^{10}
Poisson's ratio ν	0.07
Density ρ (kg/m^3)	1 490
Plie Thickness (mm)	0.22
Architecture	$[0/45_2/0/45/0]_S$

Table 1: Details and material properties for the coupons (room temperature).

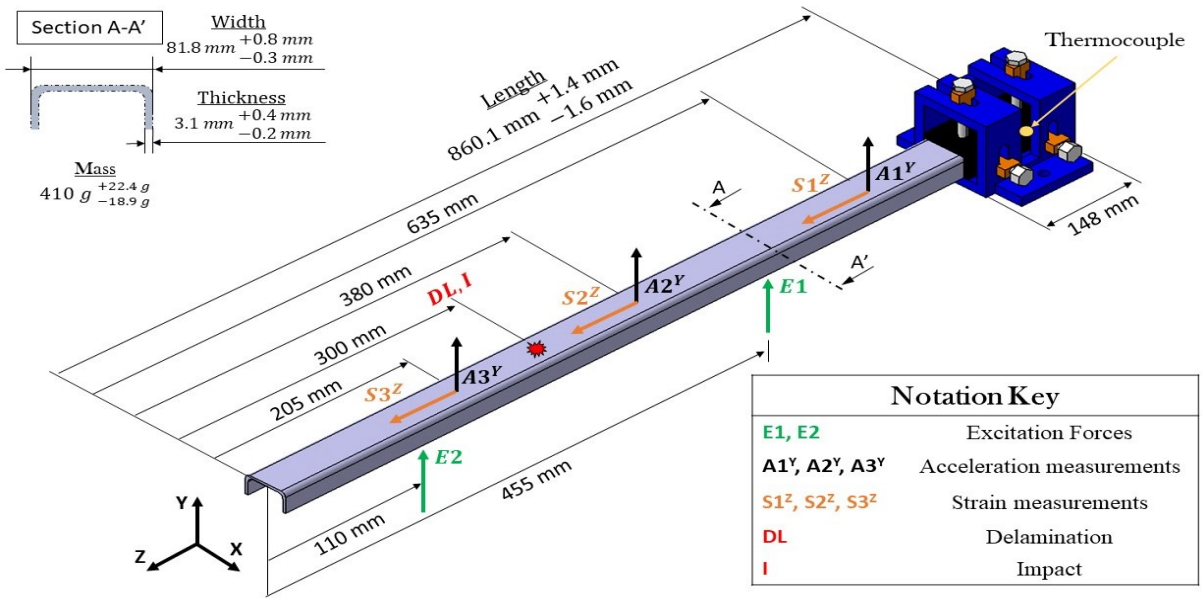

Figure 2: Schematic representation of the composite coupons indicating the damage location, the sensor locations and directions (black for acceleration, orange for strain), and the excitation locations (green). All dimensions in mm.

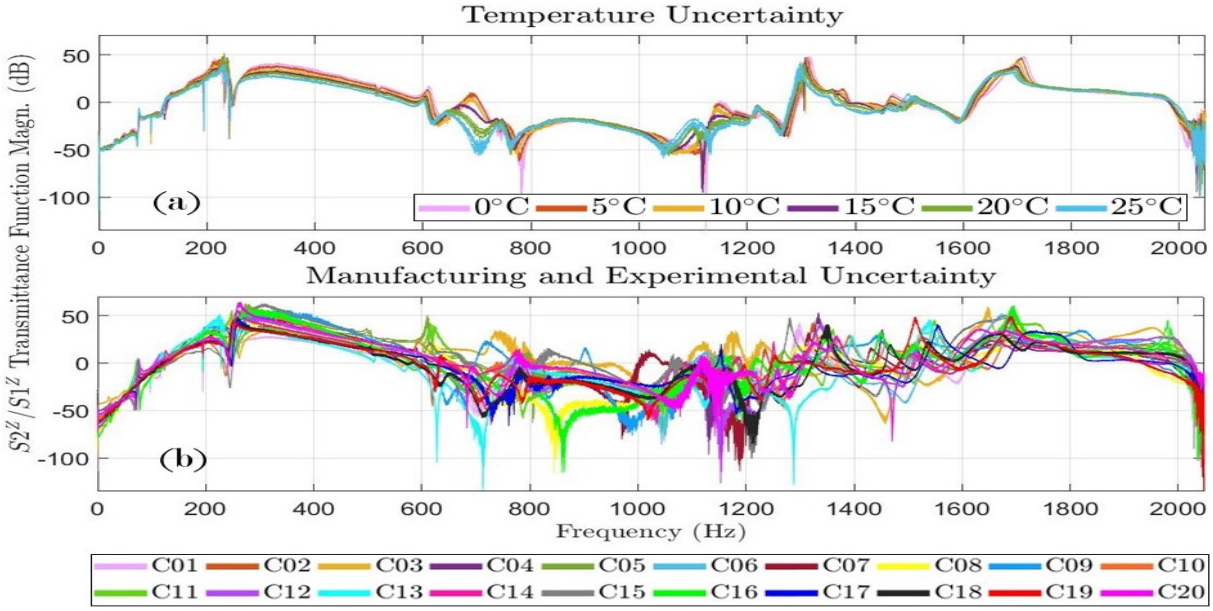

Figure 3: Effects of the uncertainty factors on the pristine structural dynamics (Welch-based MISO-TF $S2^Z/S1^Z$ magnitude estimates): (a) Temperature effects on Coupon 01 (5 curves for each one of 6 Temperatures); (b) Manufacturing and experimental uncertainty effects at the nominal Temperature of 25°C for 20 pristine coupons (5 curves per coupon).

Damage Type	Damage Level/Area	Coupon ID	Damage Scenario
Delamination$^{\diamond}$	Low (20×20 mm)	21, 22	DL_L
	High (50×50 mm)	25, 26	DL_H
Impact-Induced	Low ($13.9\,J$)	27	I_L
	High ($27\,J$)	30	I_H

$^{\diamond}$Delamination is implemented with the use of a separation layer of Teflon of the indicated, in each case, dimensions.

Table 2: The considered damage scenarios and the coupon IDs used in each one.

in between two layers at a location that is 300 mm away from the free side of the coupon (Figure 2). The delamination area is of two possible sizes: 20×20 mm for 'Low' Delamination and 50×50 mm for 'High' Delamination (notice that these areas are similar to those used in our parallel Finite Element Model based study [10], yet the damages are more serious in the present context due to the smaller size of the coupons). Impact-induced (I) damage (implemented at approximately the same location as the Delamination) is of two distinct energy levels: $12.9\,J$ for 'Low' Impact and $23.1\,J$ for 'High' Impact. Hence 4 damage scenarios are considered on six distinct coupons (see Table 2).

The effects of each damage scenario on the dynamics (presently the MISO-TF $S2^Z/S1^Z$ magnitude curves) under uncertainty are depicted in Figure 4. Evidently, the effects of all 4 damage scenarios are small compared to those of uncertainty, as their corresponding TF zones reside, almost fully, within the TF zone corresponding to the pristine dynamics under uncertainty; a fact clearly underlining the difficulty of the problem.

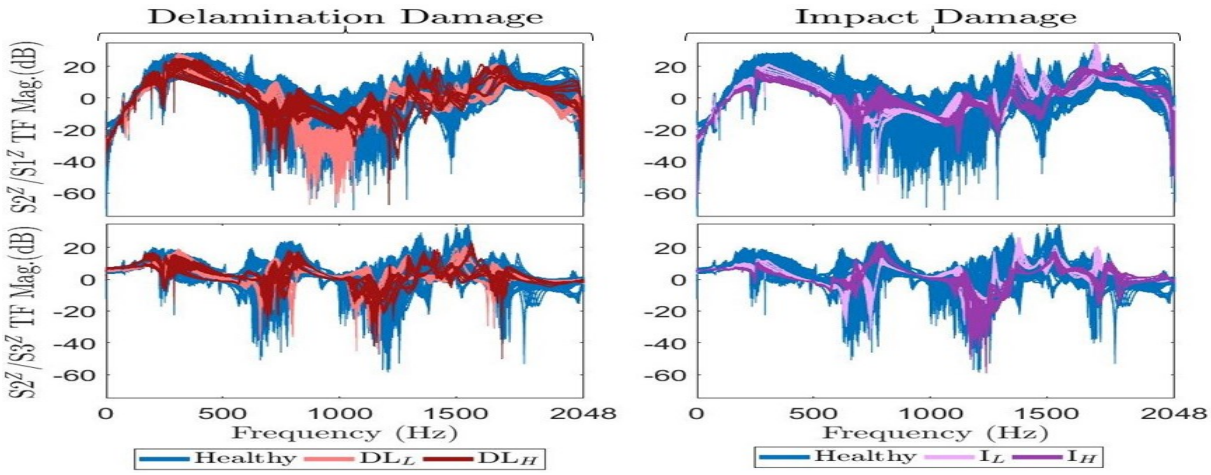

Figure 4: Effects of each Damage Scenario on Welch-based Transmittance dynamics estimates (upper row $S2^Z/S1^Z$, and lower row $S2^Z/S3^Z$ transmittance dynamics) under uncertainty: 'Low' and 'High' Delamination effects (left column), and 'Low' and 'High' Impact effects (right column). [600 sets of TF magnitude curves corresponding to 20 Pristine coupons under 6 Temperatures (blue), 120 sets of TF curves corresponding to 4 Delamination damaged coupons under 10 Temperatures (tints of red), and 60 sets of TF curves corresponding to 2 Impact damaged coupons under 10 Temperatures (purple).]

3 REMARKS ON THE ROBUST DAMAGE DIAGNOSIS METHODS

Robust *response-only* damage SHM is based on the *partial* structural dynamics, as reflected in a Multiple-Input Single-Output Transmittance Function (MISO-TF) representing the relationship among m measured response signals, with $m-1$ of them acting as pseudo-inputs and the m-th as output. The MISO-TF dynamics are represented via an AutoRegressive with eXogenous excitation (ARX) model of ARX orders (n, n), designated as an ARX(n, n) model:

$$y_m[t] + \sum_{i=1}^{n} a_i \cdot y_m[t-i] = \sum_{j=1}^{m-1} \sum_{i=1}^{n} b_i^j \cdot y_j[t-i] + w[t] \qquad w[t] \sim \text{i.i.d. } \mathcal{N}(0, \sigma_w^2) \tag{1}$$

In the above a_i $(i \in [1, n])$, b_i^j $(i \in [1, n],\ j \in [1, m-1])$ designate the model's AR and X parameters, respectively, and $w[t]$ an innovations (white) Gaussian signal, with i.i.d. standing for identically independently distributed and $\mathcal{N}(0, \sigma_w^2)$ standing for the normal (Gaussian) distribution with zero mean and variance σ_w^2. Model order selection and AR/X model parameter vector and innovations variance estimation are based on standard identification procedures using m-tuples of signals $(y_1[t], \ldots, y_m[t])$ $(t \in [1, N])$ [12]. It is noted that the use of the MISO Transmittance dynamics is important in eliminating the effect of excitation profile uncertainty provided that the number of pseudo-inputs employed equals the number of independently acting excitations.

Robust damage detection is formulated within a feature space spanned by a Principal Component Analysis (PCA) transformed and reduced version of the original ARX model parameter vector (the feature vector; details in [13]). Dimensionality reduction aims at retaining only those Principal Components that collectively explain a *minor* portion of the feature vector variability under uncertainty. It is noted that the sample covariance matrix of the original ARX parameter vector necessary for performing the PCA is based on p parameter vector estimates, each one obtained from each one of p available signal sets under the pristine structural state within the methods' Baseline/Training Phase.

Robust damage detection is based on two *unsupervised* methods using approximations of the Healthy Subspace, defined as the subspace spanned by the transformed and reduced feature vectors corresponding to the healthy dynamics under uncertainty. The first method uses a Multiple Model (MM) [13] representation of the Healthy Subspace, while the latter uses a Hyper-Sphere (HS) approximation [14]. Both representations are established in the *Baseline/Training Phase* using p signal sets under uncertainty, while damage detection takes place in the methods' *Inspection/Operational Phase*. Robust damage characterization (as Delamination or Impact-induced) is, on the other hand, based on a *supervised* MM type scheme employing cosine similarity within the original feature space (no PCA based transformation and dimensionality reduction).

4 PERFORMANCE ASSESSMENT

As two independent force excitations act on the structure, the number of pseudo-inputs is selected equal to two (the responses at locations 1 and 3 are selected, with that at location 2 serving as output). Based on the corresponding strain signals for the healthy structure under nominal conditions and standard identification procedures [12], an ARX(100,100) model is obtained for representing the MISO-TF dynamics.

Structural State	No. of Coupons	Temperatures	No. of Experiments per Temperature and Coupon	Total No. of Experiments
Baseline Phase				
Healthy	16	$\{0, 5, 10, 15, 20, 25\}^{\circ}C$	5	480
Inspection Phase				
Healthy[1]	4	$\{1, 4, 6, 9$	3	120
$DL_L + DL_H$	$2+2$	$11, 14, 16,$	3	60+60
$I_L + I_H$	$1+1$	$19, 21, 24\}^{\circ}C$	3	30+30

[1]Healthy Inspection Coupon IDs: (2,8,10,12).
Signal details: Sampling frequency $fs = 4\,096$ Hz, signal length $N = 81\,920$ samples (20 s).
Signal pre-processing includes sample mean subtraction and normalization by its sample standard deviation.

Table 3: Damage detection Baseline and Inspection Experiments.

4.1 Damage detection

In the *Baseline/Training Phase* 16 pristine coupons are employed (the *best*, most representative are selected; see the remark made in the Introduction), with 5 experiments (each one with a distinct set of force excitations) performed for each one under 6 distinct temperatures; this results into a total number of 480 Baseline Experiments (see Table 3) and a corresponding number of ARX$(100, 100)$ models. Based on the sample covariance of the ARX model parameter vector, the original parameter vector (of dimensionality 300) is PCA transformed and reduced into a dimensionality of 228 (72 PCs explaining 99.85% of parameter variability are dropped), based on which the feature space is defined and the Healthy Subspace approximations are constructed.

In the *Inspection/Operational Phase* 4 healthy and 6 damaged coupons (2 under DL_L, 2 under DL_H, 1 under I_L, and 1 under I_H) are employed, with 3 experiments (each one with a distinct set of force excitations) performed for each one under 10 distinct temperatures. This results into the total numbers of Inspection Experiments per health state indicated in Table 3).

The damage detection performance achieved by both the MM and HS based methods is assessed in Figure 5 in terms of the distance metric D of the current point in the feature space to the Healthy Subspace, and also via Receiver Operating Characteristic (ROC) curves depicting the relationship between the True Positive Rate (TPR, or correct detection rate) and the False Positive Rate (FPR, or false alarm rate). Evidently, both the MM and HS based methods achieve excellent, or almost excellent, performance for all 4 damage scenarios.

A comparison of the damage detection performance achieved by dynamic strain signals and vibration acceleration signals (from our study [11]) is presented in Figure 6 using the Accuracy (correct decision rate) index and optimal decision threshold [that is that corresponding to the point of the ROC curve that lies closest to the $(0, 1)$ point]. Evidently, the strain-based detection performance is on par with its acceleration-based counterpart for the Delamination damage scenarios (for both the MM and HS based methods) and the Impact damage scenarios (for the MM based method).

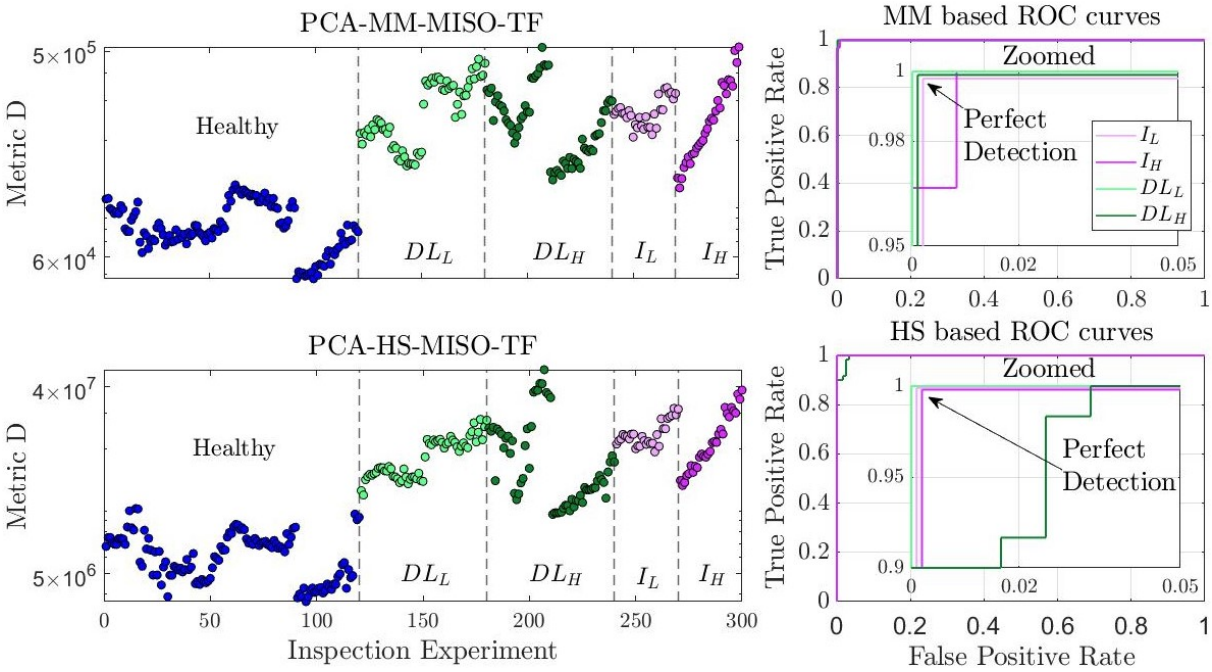

Figure 5: Robust damage detection performance for the MM (upper row) and HS (lower row) methods: Distance metric D (left column) and corresponding ROC curves (right column) based on all 300 Inspection Experiments. [Color code: Light/dark green tints for Low/High Delamination, light/dark purple tints for Low/High Impact.]

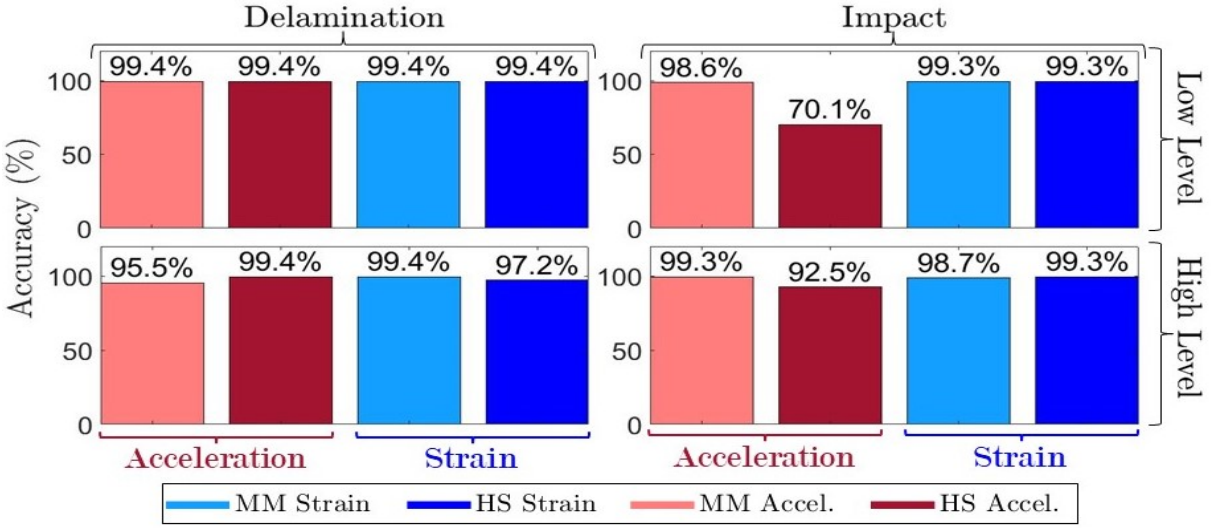

Figure 6: Strain (blue tints) versus acceleration (red tints) based robust damage detection performance: Accuracy values achieved by the MM (light tints) and HS (dark tints) methods. [Low/High (upper/lower row) Delamination/Impact (left/right column) damage scenarios; 300 Inspection Experiments.]

Structural State	Number of Coupons	Temperatures	No. of Experiments per Temperature and Coupon	Total No. of Experiments
		Baseline Phase		
Delamination	2	$\{0, 5, 10, 15, 20, 25\}°C$	5	60
Impact	1			30
		Inspection Phase		
Delamination	2	$\{1, 4, 6, 9, 11, 14, 16, 19, 21, 24\}°C$	3	60
Impact	1			30

Baseline Coupon IDs: Delamination (IDs 21, 26), Impact (ID 27).
Inspection Coupon IDs: Delamination (IDs 22, 25), Impact (ID 30).

Table 4: Damage characterization Baseline and Inspection Experiments.

4.2 Damage characterization

In the *Baseline/Training Phase*, due to the very limited number of available coupons, 1 'Low' and 1 'High' Delamination damaged coupons are employed, along with 1 'Low' Impact damaged coupon. 5 experiments (each one with a distinct set of force excitations) per each one of 6 temperatures are performed with each coupon, thus resulting into a total of 60 Baseline Experiments under Delamination and 30 under Impact (details in Table 4).

In the *Inspection/Operational Phase* 1 'Low' and 1 'High' Delamination damaged coupons are employed, along with 1 'High' Impact damaged coupon. In this case 3 experiments (each one with a distinct set of force excitations) per each one of 10 temperatures (different from those of the Baseline Phase) are performed with each coupon, thus resulting into a total of 60 Inspection Experiments under Delamination and 30 under Impact (details in Table 4).

Damage characterization is assessed via the correct characterization rate, referred to as True Positive Rate in Figure 7. As may be seen (blue bars) the characterization results are perfect, and in fact somewhat better than those obtained based on vibration acceleration signals [11] for the Impact damage scenario.

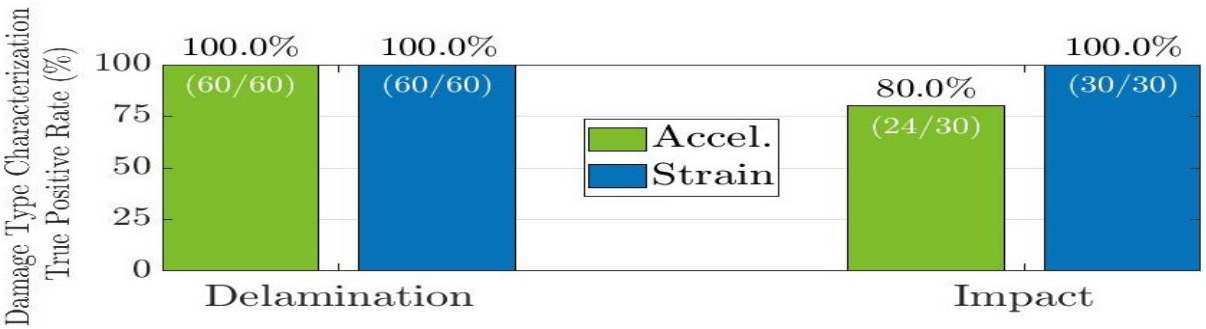

Figure 7: Strain-based (blue) versus acceleration-based (green) robust damage characterization performance: Correct characterization rates for all 60 Delamination and all 30 Impact damage Inspection Experiments.

5 CONCLUDING REMARKS

The main conclusions drawn from the study may be summarized as follows:

(i) Despite the presence of strong uncertainty, it has been experimentally demonstrated that high diagnostic performance (damage detection accuracy reaching 99.4% and almost perfect Delamination/Impact characterization) is achievable via robust *strain*-response-based SHM methods, provided that a *sufficiently large* (representative) sample of the considered population of structures is available for training.

(ii) The comparison of strain-based to acceleration-based damage diagnosis has indicated *largely similar* performance for both damage detection and characterization. This result is quite aligned with that of our Finite Element Model based parallel study [10] in which the detection performance between the two types of sensors is not particularly different for 'high' level delamination (notice that no impact type damage is considered in [10], while the two levels of delamination damage of the present study effectively are quite 'higher' than those in [10] as similar damage areas are employed for smaller structures).

Acknowledgements

The study has been carried out within the framework of the research project 'Robust to Uncertainty Machine Learning Based Structural Health Monitoring for a Population of Nominally Identical Composite Aerostructures - REALISM' (project code: T10DIS-00050, MIS 5074648) which is realized within the context of the 'Bilateral and multilateral R&T cooperation between Greece and Israel' and is co–financed by the European Regional Development Fund (ERDF) of the European Union and Greek national funds through the Operational Program Competitiveness, Entrepreneurship, and Innovation (EPAnEk).

References

[1] S. Hassani, M. Mousavi, and A. H. Gandomi, "Structural health monitoring in composite structures: A comprehensive review," *Sensors*, vol. 22, no. 1, 2022.

[2] J. Chen, B. Liu, and H. Zhang, "Review of fiber bragg grating sensor technology," *Frontiers of Optoelectronics*, vol. 4, no. 2, pp. 204–212, 2011.

[3] J. Alvarez-Montoya, A. Carvajal-Castrillón, and J. Sierra-Pérez, "In-flight and wireless damage detection in a UAV composite wing using fiber optic sensors and strain field pattern recognition," *Mechanical Systems and Signal Processing*, vol. 136, no. 106526, Feb. 2020.

[4] T. Loutas, A. Panopoulou, D. Roulias, and V. Kostopoulos, "Intelligent health monitoring of aerospace composite structures based on dynamic strain measurements," *Expert Systems with Applications*, vol. 39, no. 9, pp. 8412–8422, Jul. 2012.

[5] S. Lu, M. Jiang, Q. Sui, Y. Sai, and L. Jia, "Damage identification system of CFRP using fiber Bragg grating sensors," *Composite Structures*, vol. 125, pp. 400–406, Jul. 2015.

[6] M. Lin, S. Guo, S. He, W. Li, and D. Yang, "Structure health monitoring of a composite wing based on flight load and strain data using deep learning method," *Composite Structures*, vol. 286, no. 115305, Apr. 2022.

[7] S. Sharma, S. K. Dangi, S. K. Bairwa, and S. Sen, "Comparative study on sensitivity of acceleration and strain responses for bridge health monitoring," *Journal of Structural Integrity and Maintenance*, vol. 7, no. 4, pp. 238–251, Oct. 2022.

[8] P. Capoluongo, C. Ambrosino, S. Campopiano, A. Cutolo, M. Giordano, I. Bovio, L. Lecce, and A. Cusano, "Modal analysis and damage detection by Fiber Bragg grating sensors," *Sensors and Actuators A: Physical*, vol. 133, no. 2, pp. 415–424, 2007.

[9] X. Li, L. Wang, S. Law, and Z. Nie, "Covariance of dynamic strain responses for structural damage detection," *Mechanical Systems and Signal Processing*, vol. 95, pp. 90–105, 2017.

[10] F. T. Fera, I. E. Saramantas, P. E. Spiliotopoulos, Y. Ofir, I. Kressel, S. D. Fassois, J. S. Sakellariou, M. Tur, and C. Spandonidis, "Dynamic strain versus acceleration based robust structural health monitoring for a population of composite aerostructures under uncertainty," *Proceedings of the X ECCOMAS Thematic Conference on Smart Structures and Materials (SMART 2023)*, 2023.

[11] P. E. Spiliotopoulos, F. T. Fera, I. E. Saramantas, Y. Ofir, I. Kressel, P. Konis, I. M. Kriatsiotis, J. S. Sakellariou, S. D. Fassois, F. Giannopoulos, C. Spandonidis, and Z. Tzioridis, "Random vibration response based unsupervised damage detection for a set of composite aerostructures under varying operating conditions and uncertainty: experimental assessment," *Proceedings of the XII International Conference on Structural Dynamics (EURODYN2023)*, 2023.

[12] L. Ljung, *System Identification: Theory for the User (2nd ed.)*. Upper Saddle River, NJ 07458: Prentice Hall PTR, 1999.

[13] K. Vamvoudakis-Stefanou, J. Sakellariou, and S. Fassois, "Vibration-based damage detection for a population of nominally identical structures: Unsupervised Multiple Model (MM) statistical time series type methods," *Mechanical Systems and Signal Processing*, vol. 111, pp. 149–171, Oct. 2018.

[14] K. Vamvoudakis-Stefanou, S. Fassois, and J. Sakellariou, "An automated hypersphere-based healthy subspace method for robust and unsupervised damage detection via random vibration response signals," *Structural Health Monitoring*, vol. 21, no. 2, pp. 465–484, Mar. 2022.